Planetary and Space Science 139 (2017) 31–36

Contents lists available at ScienceDirect

Planetary and Space Science

journal homepage: www.elsevier.com/locate/pss

Evidence for detection of energetic neutral atoms by LADEE

J.J. Walker[a,*], J.S. Halekas[a,b], M. Horányi[b,c], J.R. Szalay[d], A.R. Poppe[b,e]

[a] University of Iowa, 30 North Dubuque Street, Van Allen Hall, Iowa City, IA, USA
[b] Solar System Exploration Research Virtual Institute, NASA Ames Research Center, Moffett Field, CA, USA
[c] Laboratory for Atmospheric and Space Physics, and Department of Physics, University of Colorado at Boulder, Boulder, CO, USA
[d] Southwest Research Institute, San Antonio, TX, USA
[e] Space Sciences Laboratory, University of California at Berkeley, 7 Gauss Way, Berkeley, CA, USA

ARTICLE INFO

Keywords:
Moon
Energetic neutral atoms
Solar wind
LDEX
LADEE

ABSTRACT

The integrated current of the Lunar Dust Experiment (LDEX) instrument aboard the Lunar Atmosphere and Dust Environment Explorer (LADEE) includes sources of current in addition to small (<0.3 μm) dust grains. LDEX current correlates strongly with solar wind density and flux, though solar wind ions should be excluded from the signal. Energetic neutral atoms (ENAs), produced by solar wind that is neutralized and reflected from the moon's surface, might contribute to LDEX current. To investigate this possibility, we developed a geometrical model for ENA detection. We find high correlation between predicted ENA flux and LDEX current. Based on the inverse dependence of ENA detection sensitivity on solar wind speed, we exclude sputtering from the spherical surface inside the instrument as the mechanism for ENA detection. Additionally, we observe a drop in LDEX current that is consistent with a drop in th]e predicted ENA flux associated with a lunar magnetic anomaly (LMA) centered at -178°E and 6°N selenographic longitude and latitude, respectively. This provides additional confirmation that ENAs are the main contributor to the LDEX current rather than ions, because the ENA flux decreases in LMA regions and reflected hydrogen ion flux increases in LMA regions.

1. Introduction

LDEX was developed to explore dust populations in the lunar exosphere (Horányi et al., 2014). LDEX is an impact ionization dust detector capable of individually detecting grains with radii > 0.3 μm. LDEX used an integrated current mode to search for the putative population of <0.3 μm submicron grains that might contribute to the lunar horizon glow originally observed by the Apollo astronauts and by Lunar Surveyor (McCoy and Criswell, 1974; McCoy, 1976). This integrated current mode operates by subtracting the current measurement made in the switched mode from the current measurement made in the nominal mode. In the nominal mode, an inner hemispherical grid is biased 200 Volts negative with respect to a hemispherical target (held at the chassis ground), which collects ions of all energies. In the switched mode, this hemispherical grid is biased 30 Volts positive with respect to the target, preventing ions with energy less than 30 eV from reaching the Micro Channel Plate (MCP) and being detected. In the switched mode, solar wind ions possess high enough energy that they are collected. Because the solar wind ions are present in both the nominal and switched modes, when the switched current is subtracted from the nominal current, the solar wind contribution is removed from the signal.

Ultimately, the density of submicron grains is far too small to produce lunar horizon glow in the altitude range of 3–250 km above the lunar surface (Horányi et al., 2015; Szalay and Horányi, 2015). The lack of altitude dependence of the dust density upper bound limit implies low energy solar wind ions are responsible for a significant fraction of the current (Szalay and Horányi, 2015). Szalay et al. found that the LDEX current correlates closely with the solar wind density in the terminator region, quoting a correlation coefficient as high as 0.64 (Szalay and Horányi, 2015). This is puzzling, because high energy solar wind ions should, in principle, be excluded from the LDEX current measurement.

There are a few possibilities that might couple solar wind to LDEX current, such as back-scattered protons or ENAs (Xie et al., 2016). A significant fraction (≈ 20%) of the solar wind is reflected from the lunar surface as ENAs (Wieser et al., 2009; McComas et al., 2009; Lue et al., 2016), although 16% is the global average as found by mapping studies (Vorburger et al., 2013). Because the fraction of solar wind that is reflected as ions in non-magnetic regions is <1% (Saito et al., 2008, 2010; Lue et al., 2014), which is much smaller than the fraction reflected as ENAs, ENAs appear to be the best candidate to connect

* Corresponding author.
E-mail address: jeffrey-walker@uiowa.edu (J.J. Walker).

http://dx.doi.org/10.1016/j.pss.2017.03.002
Received 9 July 2016; Accepted 3 March 2017
Available online 08 March 2017
0032-0633/

solar wind flux and LDEX current. Pick up ions in the lunar exosphere (Poppe et al., 2012) provide an additional source of particle flux to the LDEX detector, and Poppe et al. were able to measure these pick up ions in the integrated current (Poppe et al., 2016). To eliminate the influence of pick up ions on the LDEX signal, isolating the times where we expect the current to arise from ENAs alone, we only model the portions of the data set where the convective electric field is less than 90° relative to the LDEX boresight. Because the largest portion of ENAs are reflected from the sunlit portion of the moon, we focus on mission data between 6 and 18 h lunar local time. We note that LDEX only operated between 6 and 12 h local while ram pointed, due to instrument constraints while sun-pointing. In our analysis we also include the times when LDEX operates while anti-ram pointed, hence we are able to include LDEX measurements between 6 and 18 h lunar local time. We also restrict our analysis to times when the moon is outside the earth's magnetotail and magnetosheath by excluding between 135° and 225° in Geocentric Solar Ecliptic (GSE) coordinates to minimize the complications of ENA behavior.

2. Geometrical model of ENA Flux

Schaufelberger et al. provide an analytical model for the scattering function f_s of energetic neutral hydrogen as a function of solar zenith angle and scattering angles (Schaufelberger et al., 2011). Specifically, the directional ENA flux in units of number $\cdot m^{-2} sr^{-1} s^{-1}$ can be described by

$$j_{ENA}(SZA, \phi, \theta) = J_{SW} \cdot R_{\perp} f_s(SZA, \phi, \theta), \quad (1)$$

where J_{SW} is the solar wind flux in units of number /(m^2s), $f_s(SZA, \phi, \theta)$ is the scattering function in units of 1/sr, SZA is the solar zenith angle, ϕ is the azimuthal scattering angle, θ is the polar scattering angle, and $R_{\perp} = J_{ENA}/J_{SW}$ is the ratio between the total reflected ENA flux and the incident solar wind flux at the sub-solar point. Integration of the directional flux $j_{ENA}(SZA, \phi, \theta)$ over all scattering and solar zenith angles results in the total flux of ENAs from the lunar surface, J_{ENA}.

LDEX has a wide field of view, accepting ENAs from a large range of scattering angles and positions on the lunar surface. Fig. 1 shows the LDEX field of view over the lunar surface. We include all sight lines extending outward from LDEX at 3° intervals relative to the boresight direction that are within 90° of the LDEX boresight and at 4° intervals in the azimuthal direction. This array may include ENA trajectories that are not likely to strike the LDEX instrument, such as trajectories that are nearly perpendicular to the LDEX boresight direction, but such rays are

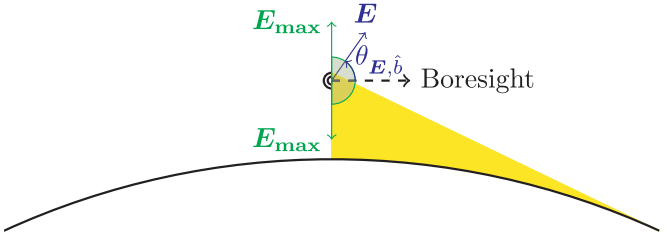

Fig. 1. Diagram of the LDEX field of view over the lunar surface. The large, black arc on the bottom of the figure shows the lunar surface, and the two black, concentric semi-circles directly above it represent the LDEX instrument, with the outer black semi-circle representing the target and the inner black semi-circle representing the hemispherical biasing grid (see Fig. 2 for the diagram of LDEX). The dashed black arrow shows the boresight direction, while the blue arrow shows the electric field direction, which is in general a function of time ($\mathbf{E}(t) = -\mathbf{v}(t) \times \mathbf{B}(t)$). The arced blue arrow represents $\theta_{\mathbf{E},\hat{b}}$, the time-dependent angle between the boresight and electric field. We indicate the allowed range for the electric field used in our data subset relative to the boresight direction by the green, shaded semi-circle, bounded by the two green arrows $\mathbf{E}_{max}$. The maximum allowed angle of $\theta_{\mathbf{E},\hat{b}}$ is 90°; the green semi-circle is displayed as a result of the azimuthal symmetry around the boresight vector. The yellow cone shows the boundary of all sightlines from LDEX that intersect the lunar surface. In this diagram, the boresight vector is aligned with the ram direction of the spacecraft. (For interpretation of the references to color in this figure legend, the reader is referred to the web version of this article).

practically excluded when a relevant response function is used, as discussed shortly. For any of these rays that strike the lunar surface, we compute their solar zenith and scattering angles. We calculate the fractional flux for each of these rays according to $f_s(SZA, \phi, \theta)$. This number, calculated for each interrogation ray and multiplied by an ad hoc angular response function for LDEX (discussed below), represents the fraction of the total ENA flux/J_{SW} that strikes the LDEX instrument. We add up the contribution from all interrogation rays that strike the lunar surface.

The LDEX angular response function to ENAs is unknown, because the instrument was designed for dust detection without consideration for ENAs. Because scattering from instrument surfaces is potentially involved this is not just a straightforward geometrical response function that could have been measured in the lab without an ENA source. Therefore, we assume a basic gaussian response as our model,

$$f_r(\theta_l) = \frac{\sqrt{\frac{\ln 2}{\pi}}}{\theta_w} \exp\left[-\ln 2\left(\frac{\theta_l - \theta_c}{\theta_w}\right)^2\right], \quad (2)$$

where f_r is the angular response function, θ_w is the half of the width at half maximum in degrees, representing how wide or narrow LDEX angular sensitivity is to ENA detection, θ_l is the angle of a given interrogation ray with respect to the boresight in degrees, and θ_c is the offset of the response function with respect to the boresight in degrees. Choosing $\theta_c = 0$, for example, produces a response function that is more sensitive to ENAs incident along the LDEX boresight. See Fig. 2 for a graphical representation of the angular response function. We do not suggest that the response function must be gaussian, but rather, we use this as a simple model to provide insight as to whether the LDEX instrument is more sensitive to ENAs along the boresight or at some oblique angle.

The result of adding up the contributions of all interrogation rays, multiplied by the angular sensitivity function for their angle with respect to the boresight and a factor for the element of solid angle corresponding to the interrogation ray, produces the total incident ENA flux. We essentially perform a numerical integration of

$$\int j_{ENA}(\theta_l) f_r(\theta_l) d\Omega = \int j_{ENA}(\theta_l) f_r(\theta_l) 2\pi \sin\theta_l d\theta_l = 2\pi J_{SW} \cdot R_{\perp} \int f_s(\theta_l) f_r(\theta_l) \sin\theta_l d\theta_l, \quad (3)$$

where $j_{ENA}(\theta_l)$ is the contribution of directional ENA flux from an interrogation ray at an angle θ_l relative to the boresight vector, $d\Omega = d\varphi_l \sin\theta_l d\theta_l$ is an element of solid angle, φ_l is the azimuthal viewing angle relative to LDEX, and integration over φ_l produces a factor of 2π. This process produces the flux (m^{-2} s^{-1}) because the integration over the LDEX field of view is equivalent to integration over the range of solar zenith and scattering angles sampled by LDEX. However, we cannot determine exactly the number of ENAs incident on the target surface since the LDEX efficiency and effective area are unknown. We therefore scale our results to match the magnitude of the observed LDEX integrated current. For clarity, we refer to the integral of scattering and angular response functions as the geometrical ENA model. We refer to the product of solar wind flux and reflection ratio with the geometrical ENA model as ENA flux.

Fig. 3 shows the ENA model and ENA flux scaled to match the magnitude of the observed LDEX integrated current in e/s, where e is the elementary charge. The geometrical ENA model closely follows the LDEX data over the timescale of a LADEE orbit, with a correlation coefficient of 0.86 between the model and the LDEX integrated current for the orbits shown in Fig. 3. The ENA flux to the LDEX instrument depends not only on the scattering function and LDEX field of view, but should be multiplied by the solar wind flux as measured by ARTEMIS (Angelopoulos, 2010) and the global reflection ratio. The correlation coefficient between LDEX current and ENA flux is 0.89 for the orbits shown in Fig. 3.

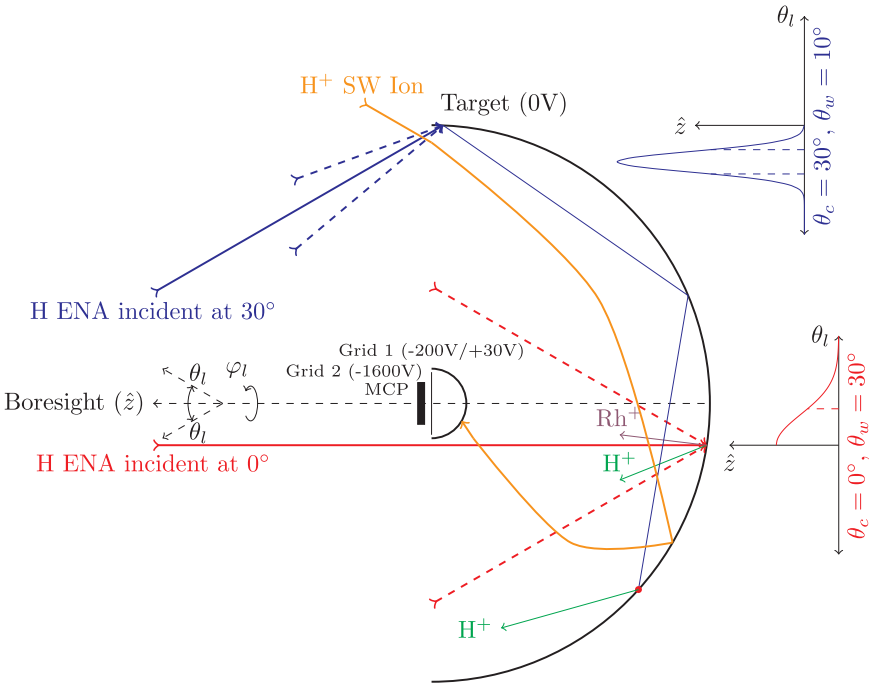

Fig. 2. Diagram of ENAs incident on the LDEX instrument. The Rhodium target is the grounded, larger semi-circle. The inner radial electrode (grid 1) is the smaller semi-circle. A planar grid (grid 2) accelerates ions that reach the inner radial electrode toward the MCP. The angle with respect to the boresight vector is represented by θ_l, and the azimuthal angle is represented by φ_l. The orange line shows an example solar wind ion that enters the instrument in the annular region between the inner radial electrode (grid 1) and the target, and once inside the instrument, the radial electric field between the target and the inner radial electrode causes this ion to be collected. The solid red line shows an example ENA incident at zero degrees with respect to the boresight and the solid blue line shows an example ENA incident at thirty degrees with respect to the boresight. The dashed lines on either side of these two rays show example ENAs incident at angles corresponding to the full width at half max for the two angular response functions shown. The short purple line shows a low energy sputtered Rhodium ion (Rh^+) resulting from an incident ENA. The short green lines show Hydrogen ions (H^+) resulting from ENAs ionizing due to impact with the target surface. We have used the ENA incident at thirty degrees as an example of how an ENA may reflect specularly multiple times (shown by the thinner blue lines inside LDEX) before ionizing to become a lower energy H^+ ion. The azimuthally symmetric angular response functions are plotted for each case, where the full width at half max is shown by horizontal dashed lines. (For interpretation of the references to color in this figure legend, the reader is referred to the web version of this article).

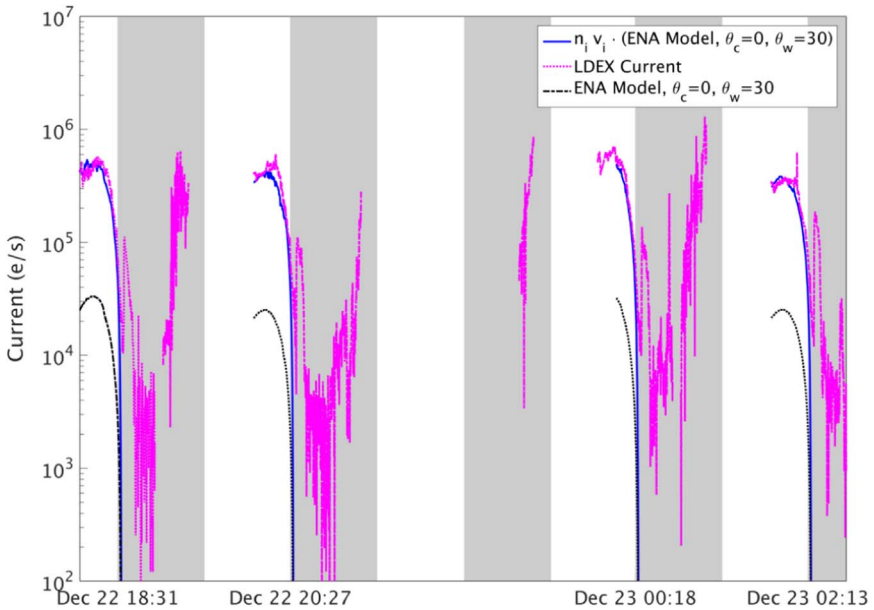

Fig. 3. Example showing the close visual match between the LDEX integrated current and the geometrical model for ENA flux. LDEX measurements are from December 2013 and timestamps in the figure are given in UTC. Gray vertical bars indicate the times where LADEE is in the lunar optical shadow. Model data is only shown when the electric field relative to boresight is less than 90°. The magenta dotted line shows the LDEX integrated current measurements in units of e/s. The black dash-dot line shows the geometrical ENA model, assuming a gaussian angular response function with $\theta_c = 0°$ and $\theta_w = 30°$, multiplied by the global ENA reflection ratio of 0.16, and scaled by a factor 10^7. The solid blue line shows the geometrical ENA model multiplied by the solar wind flux and the global ENA reflection ratio of 0.16, yielding the predicted ENA flux, with the result in units of $m^{-2}s^{-1}$. This is further scaled by a factor 5×10^{-4} in order to match the magnitude of the LDEX current measurements. LDEX current exists in the optical shadow due to the effects of spacecraft charging. When the spacecraft is behind the moon, the spacecraft charges negatively, attracting low energy ions. There is no LDEX data for the period when LADEE is on the sunlit side of the moon after the December 22, 20:27 UTC time marking in this figure because LDEX is sunward pointing during this time. LDEX is not powered at any time when it is sunward pointing in order to prevent detector saturation. (For interpretation of the references to color in this figure legend, the reader is referred to the web version of this article).

3. Model results

Fig. 3 displays great qualitative agreement between ENA flux and the LDEX integrated current for several orbits. To fully assess our model as a viable candidate to explain the LDEX current, we should find the correlation coefficient for the entire mission. Fig. 4 shows cross-correlations between the LDEX current and solar wind density, LDEX current and solar wind flux, and LDEX current and ENA flux. We find a high correlation between solar wind density and the LDEX current at a time lag of zero over the entire mission, though slightly lower than the value 0.64 found by Szalay et al. near the dawn terminator (5:30–6:30 LT) (Szalay and Horányi, 2015). The coefficient increases when comparing solar wind flux and LDEX integrated current. We obtain the best correlations when comparing LDEX current and ENA flux, validating our model. Of the different models tested for the angular sensitivity of LDEX to ENAs, we find that a gaussian response centered at 30 degrees with half width half max of 10 degrees correlates best with LDEX integrated current.

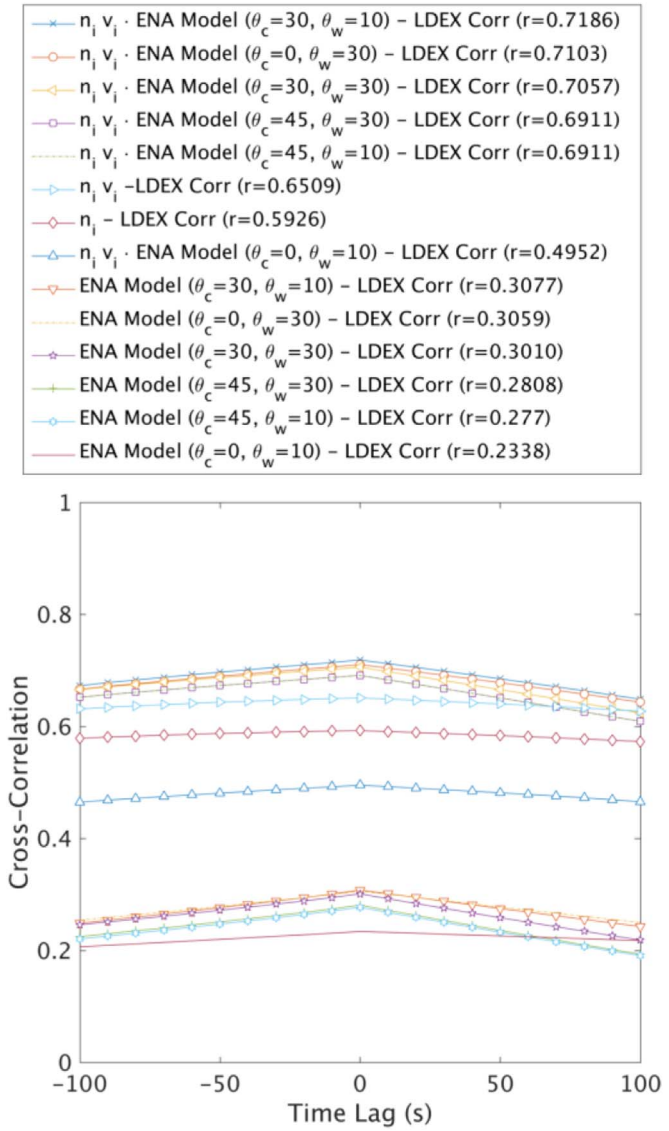

Fig. 4. Cross-correlation between various angular response functions within the geometrical ENA model and the LDEX integrated current. Correlation coefficients are listed in the legend in descending numerical order. To find these correlations, we restricted the dataset to include only times where LADEE is between 6 and 18 h lunar local time, the moon is between 135° and 225° in GSE coordinates, and for electric field relative to boresight angles less than 90°.

In our analysis, we noted occasional recurring dips in the LDEX integrated current (by nearly a factor of two) that did not appear to be connected with solar wind fluctuations. Fig. 5 shows the LDEX current of a notable case for two successive orbits with this characteristic. We note the curious similarity of this particular feature to ENA measurements of an LMA made by Vorburger et al. (2012). Reflection of solar wind ions from these features locally decreases ENA production, leading to depletions of measured ENA fluxes in these areas (Wieser et al., 2010). To test the hypothesis that this feature corresponds to an observation of an LMA, we looked for possible candidates visible to LDEX along its orbit using the Lunar Prospector maps (Mitchell et al., 2008). The small region near − 178° east longitude and 6° north latitude is the only anomaly with appreciable lines of sight to the LDEX instrument during the orbits where we see the recurring dip in LDEX current. The magnetic field is between 24 and 52 nT in this small region, which might conceivably reduce the ENA flux to the LDEX instrument when LADEE flies over. To include this anomaly in our model, we specified a global value for ENA reflection ratio $R_\perp$, and a separate, smaller value of $R_\perp$ for the region of higher magnetic field in the LMA. We used 0.16 for the global value of $R_\perp$, and the lower value $R_\perp = 0.12$ for interrogation rays that strike the lunar surface between − 176° and −180 ° east longitude, and 4° and 8° north latitude.

As seen in Fig. 5, no dip occurs in the ENA model when the value of $R_\perp = 0.16$ is held constant over the lunar surface. The dip in the geometrical model appears, coincident with the dip in LDEX current, when including interrogation rays originating from the LMA with a lower reflection ratio. We also see this feature in the predicted ENA flux, showing that this feature is not just a dip in solar wind flux. Both examples of LDEX encountering the magnetic anomaly show LDEX current greater than the model prediction at the trailing edge. We note that our simplistic model, where the anomaly region has a uniform, but lower reflection ratio, does not fully represent the behavior of the lunar surface. We note that it is also possible to observe enhancements in ENA flux as the spacecraft passes over the trailing edge of the anomaly. For example, Wieser et al., (2010) reported an enhanced energetic neutral hydrogen flux in an annular region around a magnetic anomaly.

The dip in LDEX current that is concurrent with the predicted dip in ENA flux near the −178 degrees east longitude and 6 degrees north latitude LMA is just one such feature of the LDEX data set. Since LADEE orbits many times over some of these magnetic anomalies, it might be possible to investigate the solar wind interaction with LMAs using the LDEX dataset.

4. Discussion

The high correlation between the ENA flux and LDEX current over the entire mission raises the question of how ENAs contribute to the current. ENAs, being neutral, cannot directly contribute to the current unless they scatter from the target into the MCP, or if they sputter target material to the MCP. ENAs reflected directly from the target to the MCP without ionizing should not contribute to the residual current, since these neutrals strike the detector in both the nominal mode and switched mode. Sputtering of neutral Rhodium atoms should also not be responsible, since their signal would be detected in both modes of LDEX operation and thereby be subtracted. This leaves two possible ways in which ENAs contribute to the current, either the sputtering of low energy (<30 eV) Rh^+ from the target to the MCP, or through ionization within the instrument of incident ENAs impacting the target surface and subsequent scattering to the target. Analyzing velocity dependence of the product of ENA detection efficiency and effective area (LDEX integrated current divided by ENA flux) may discriminate which of these two mechanisms is primarily responsible for the residual current. We know that ENA energy increases when the solar wind speed increases (Futaana et al., 2012). Incident ENAs should sputter increasingly more low energy Rh^+ atoms as the ENA energy increases, hence the detection efficiency should increase with solar wind speed (Biersack

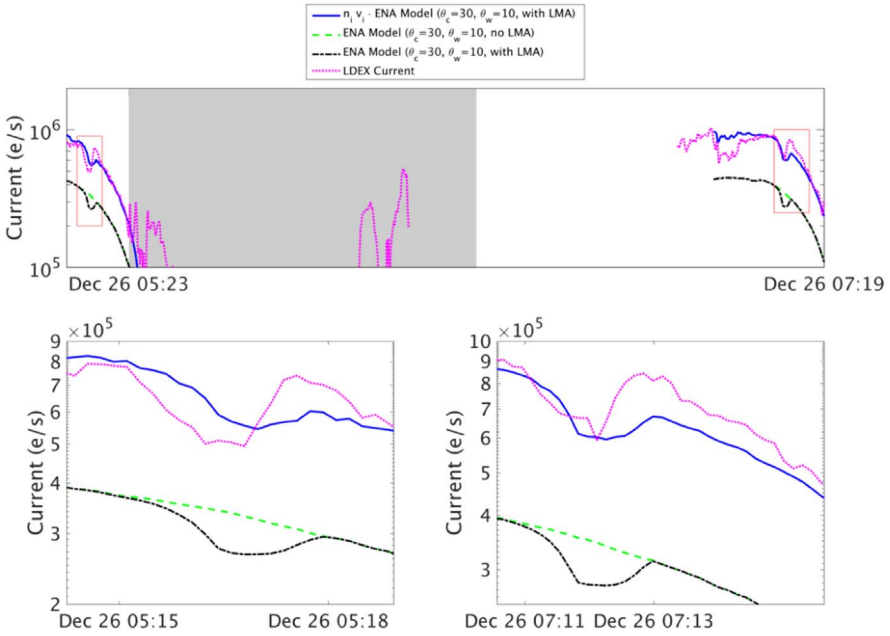

Fig. 5. Example of mission data consistent with ENA flux prediction for lunar magnetic anomaly near − 178° east longitude and 6° north latitude. LDEX current measurements, shown as the magenta dotted line in units of e/s, are from December 2013, and timestamps in the figure are given in UTC. Gray vertical bars indicate the times where LADEE is in the lunar optical shadow. Model data is only shown when the electric field relative to boresight is less than 90°. The dashed green line shows the geometrical ENA model amplitude when the ENA reflection constant is held at 0.16, multiplied by an arbitrary factor of 3×10^8. The dash-dot black line shows the geometrical ENA model amplitude when interrogation rays that strike the lunar surface between − 176° and − 180° are given the value 0.12, and all other interrogation rays are given the value 0.16. This is also multiplied by an arbitrary factor of 3×10^8. The solid blue line shows the product of the solar wind flux with geometrical ENA model, including the effect of the lunar magnetic anomaly, predicting the ENA flux in units of $m^{-2}s^{-1}$. The predicted ENA flux is reduced by a factor of 2×10^{-4} to overlay with LDEX current. The LMA-relevant regions of the upper panel are highlighted by red boxes and expanded views of these two regions are shown in the two lower panels. The large drop in LDEX current seen in the second orbit before the red box is solely due to fluctuations in solar wind flux, not a signature of an LMA. In the top panel, LDEX current exists in the optical shadow due to the effects of spacecraft charging. When the spacecraft is behind the moon, the spacecraft charges negatively, attracting low energy ions. (For interpretation of the references to color in this figure legend, the reader is referred to the web version of this article).

and Eckstein, 1984). By contrast, only the ENA population with less than 30 eV can contribute to the LDEX current by ionization and scattering. Differential flux measurements suggest an energy distribution with a peak near 100 eV (Futaana et al., 2012). Increasing solar wind speed shifts the energy peak to higher energies, and the population of ENAs below 30 eV decreases.

Fig. 6 shows a plot of the product of LDEX detector efficiency and effective area as a function of solar wind speed for the entire mission. Each data point is obtained by computing the orbit-averaged value of LDEX current divided by the ENA flux. We use the orbit-averaged value to reduce fluctuation in this quantity. In Fig. 6, the product of efficiency and area decreases as a function of solar wind speed. Based on this inverse dependence, we rule out sputtering as the mechanism for ENA detection. The ENA ionization and scattering mechanism appears consistent with the relationship shown in Fig. 6. An additional piece of evidence is that the response function with oblique incidence angle $\theta_c = 30°$ and the smaller half width, half maximum tested of $\theta_w = 10°$ in Fig. 4 shows the highest correlation with the LDEX integrated current. ENAs entering at a narrow range of oblique angles and with low enough energies (≈ 30 eV) may end up reflecting off the rhodium surface of the target several times, producing multiple opportunities to ionize and subsequently enter the MCP, as illustrated in Fig. 2.

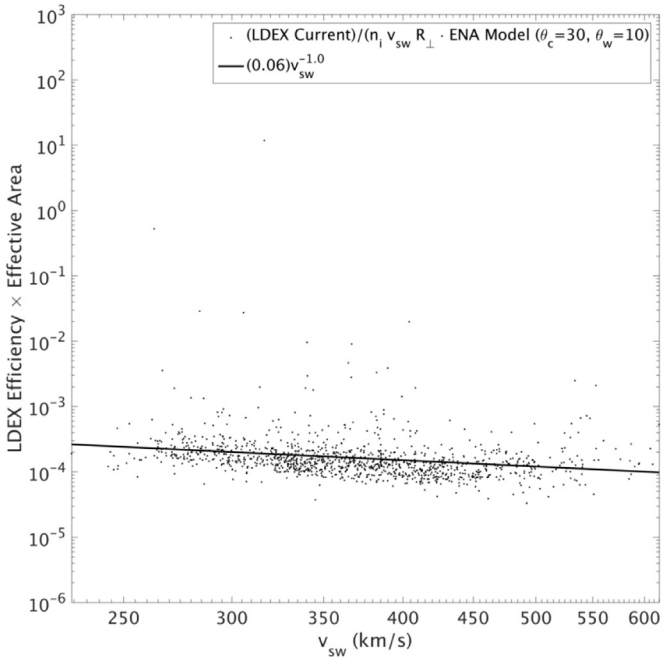

Fig. 6. Product of efficiency of ENA detection in LDEX and effective collection area of LDEX. Each black dot shows the LDEX current divided by the predicted ENA flux, where the ENA flux is the product of solar wind flux, the global ENA reflection ratio $R_\perp = 0.16$, and the amplitude of the geometrical ENA model with $\theta_c = 30$, $\theta_w = 10$. The effect of LMAs are not included. Each of these data points show an average of the LDEX current to ENA flux ratio over a LADEE orbit. When we perform the orbit average, we exclude data points during a LADEE orbit where the electric field relative to boresight is greater than 90°, LADEE is in the lunar optical shadow, or the moon is between 135° and 225° in GSE coordinates. The solid line shows a power law fit for comparison.

5. Conclusion

We have shown that the signal from a geometrical model for ENA flux detection by the LDEX instrument strongly correlates with the LDEX integrated current. The correlation between the integrated LDEX current and the ENA flux is higher than with the ion density or solar wind flux alone. Additionally, of the models used for LDEX angular sensitivity, we find that the gaussian response centered at 30° with respect to LDEX boresight and with half width half maximum of 10° provides the highest correlation to the LDEX current. We rule out

sputtering as the mechanism for ENA detection by LDEX due to the inverse dependence of the product of detection efficiency and effective area on the solar wind speed. We favor the hypothesis that oblique incidence of ENAs into the LDEX instrument lead to successive scattering events where ENAs lose energy, ionize, and become detected by LDEX after the background signal subtraction. We also report here for the first time the presence of recurring signatures of lunar magnetic anomalies present in the LDEX dataset. Because LDEX appears to be a strong detector of ENAs, the integrated current in combination with the geometrical model might be used to produce maps of ENA reflection ratios in the style of Vorburger et al. (2013), help find an upper bound on submicron dust density in the lunar exosphere, provide additional ENA measurements of lunar magnetic anomalies, and investigate solar wind interaction with lunar magnetic anomalies.

Acknowledgments

LADEE LDEX data is available online in NASA's planetary data system and ARTEMIS data are available at http://artemis.ssl.berkeley.edu. Funding: This work was supported by NASA grant NNX14AR24G, with partial support by SSERVI.

References

Angelopoulos, V., 2010. The ARTEMIS mission. Space Sci. Rev. 165 (1), 3–25. (URL: ⟨http://dx.doi.org/10.1007/s11214-010-9687-2⟩).

Biersack, J.P., Eckstein, W., 1984. Sputtering studies with the monte carlo program trim.sp. Appl. Phys. A 34 (2), 73–94. (URL: ⟨http://dx.doi.org/10.1007/BF00614759⟩).

Futaana, Y., Barabash, S., Wieser, M., Holmström, M., Lue, C., Wurz, P., Schaufelberger, A., Bhardwaj, A., Dhanya, M.B., Asamura, K., 2012. Empirical energy spectra of neutralized solar wind protons from the lunar regolith. J. Geophys. Res.: Planets 117 (E5), E05005. (URL: ⟨http://dx.doi.org/10.1029/2011JE004019⟩.).

Horányi, M., Sternovsky, Z., Lankton, M., Dumont, C., Gagnard, S., Gathright, D., Grün, E., Hansen, D., James, D., Kempf, S., Lamprecht, B., Srama, R., Szalay, J., Wright, G., 2014. The lunar dust experiment (LDEX) onboard the lunar atmosphere and dust environment explorer (LADEE) mission. Space Sci. Rev. 185 (1–4), 93–113. (URL: ⟨http://dx.doi.org/10.1007/s11214-014-0118-7⟩).

Horányi, M., Szalay, J.R., Kempf, S., Schmidt, J., Grün, E., Srama, R., Sternovsky, Z., 2015. A permanent, asymmetric dust cloud around the moon. Nature 522, 322–333. (URL: ⟨http://dx.doi.org/http://dx.doi.org/10.1038/nature14479⟩).

Lue, C., Futaana, Y., Barabash, S., Wieser, M., Bhardwaj, A., Wurz, P., 2014. Chandrayaan-1 observations of backscattered solar wind protons from the lunar regolith: dependence on the solar wind speed. J. Geophys. Res.: Planets 119 (5), 968–975. (URL: ⟨http://dx.doi.org/10.1002/2013JE004582⟩.).

Lue, C., Futaana, Y., Barabash, S., Saito, Y., Nishino, M., Wieser, M., Asamura, K., Bhardwaj, A., Wurz, P., 2016. Scattering characteristics and imaging of energetic neutral atoms from the moon in the terrestrial magnetosheath. J. Geophys. Res.: Space Phys. 121 (1), 432–445. (2015JA021826 URL: ⟨http://dx.doi.org/10.1002/2015JA021826⟩).

McComas, D.J., Allegrini, F., Bochsler, P., Frisch, P., Funsten, H.O., Gruntman, M., Janzen, P.H., Kucharek, H., Möbius, E., Reisenfeld, D.B., Schwadron, N.A., 2009. Lunar backscatter and neutralization of the solar wind: first observations of neutral atoms from the moon. Geophys. Res. Lett. 36 (12), l12104. (L12104 URL:⟨http://dx.doi.org/10.1029/2009GL038794⟩.).

McCoy, J.E., Criswell, D.R., 1974. Evidence For Lunar Dust Atmosphere From Apollo Orbital Observations. In: Lunar and Planetary Science Conference, Vol. 5 of Lunar and Planetary Science Conference.

McCoy, J.E., 1976. Photometric studies of light scattering above the lunar terminator from Apollo solar corona photography. In: Merrill, R.B. (Ed.), Lunar and Planetary Science Conference Proceedings, Vol. 7 of Lunar and Planetary Science Conference Proceedings, pp. 1087–1112.

Mitchell, D., Halekas, J., Lin, R., Frey, S., Hood, L., Acuña, M., Binder, A., 2008. Global mapping of lunar crustal magnetic fields by lunar prospector. Icarus 194 (2), 401–409. (URL: ⟨http://www.sciencedirect.com/science/article/pii/S0019103507005829 http://dx.doi.org/http://dx.doi.org/10.1016/j.icarus.2007.10.027⟩.).

Poppe, A.R., Samad, R., Halekas, J.S., Sarantos, M., Delory, G.T., Farrell, W.M., Angelopoulos, V., McFadden, J.P., 2012. ARTEMIS observations of lunar pick-up ions in the terrestrial magnetotail lobes. Geophys. Res. Lett. 39 (17), l17104. (L17104 ⟨http://dx.doi.org/10.1029/2012GL052909⟩.).

Poppe, A.R., Halekas, J.S., Szalay, J.R., Horányi, M., Levin, Z., Kempf, S., 2016. Ladee/ldex observations of lunar pickup ion distribution and variability. Geophys. Res. Lett.. (306930772016GL068393 URL:⟨http://dx.doi.org/10.1002/2016GL068393⟩.).

Saito, Y., Yokota, S., Tanaka, T., Asamura, K., Nishino, M.N., Fujimoto, M., Tsunakawa, H., Shibuya, H., Matsushima, M., Shimizu, H., Takahashi, F., Mukai, T., Terasawa, T., 2008. Solar wind proton reflection at the lunar surface: low energy ion measurement by MAP-PACE onboard SELENE (KAGUYA). Geophys. Res. Lett. 35 (24), l24205. (L24205 URL: ⟨http://dx.doi.org/10.1029/2008GL036077⟩.).

Saito, Y., Yokota, S., Asamura, K., Tanaka, T., Nishino, M.N., Yamamoto, T., Terakawa, Y., Fujimoto, M., Hasegawa, H., Hayakawa, H., Hirahara, M., Hoshino, M., Machida, S., Mukai, T., Nagai, T., Nagatsuma, T., Nakagawa, T., Nakamura, M., Oyama, K.-i., Sagawa, E., Sasaki, S., Seki, K., Shinohara, I., Terasawa, T., Tsunakawa, H., Shibuya, H., Matsushima, M., Shimizu, H., Takahashi, F., 2010. In-flight performance and initial results of plasma energy angle and composition experiment (PACE) on SELENE (kaguya). Space Sci. Rev. 154 (1), 265–303. (URL: ⟨http://dx.doi.org/10.1007/s11214-010-9647-x⟩.).

Schaufelberger, A., Wurz, P., Barabash, S., Wieser, M., Futaana, Y., Holmström, M., Bhardwaj, A., Dhanya, M.B., Sridharan, R., Asamura, K., 2011. Scattering function for energetic neutral hydrogen atoms off the lunar surface. Geophys. Res. Lett. 38 (22), l22202. (L22202 URL: ⟨http://dx.doi.org/10.1029/2011GL049362⟩).

Szalay, J.R., Horányi, M., 2015. The search for electrostatically lofted grains above the moon with the lunar dust experiment. Geophys. Res. Lett. 42 (13), 5141–5146. (URL: ⟨http://dx.doi.org/10.1002/2015GL064324⟩).

Vorburger, A., Wurz, P., Barabash, S., Wieser, M., Futaana, Y., Holmström, M., Bhardwaj, A., Asamura, K., 2012. Energetic neutral atom observations of magnetic anomalies on the lunar surface. J. Geophys. Res.: Space Phys. 117 (A7), A07208. (a07208 URL: ⟨http://dx.doi.org/10.1029/2012JA017553⟩).

Vorburger, A., Wurz, P., Barabash, S., Wieser, M., Futaana, Y., Lue, C., Holmström, M., Bhardwaj, A., Dhanya, M.B., Asamura, K., 2013. Energetic neutral atom imaging of the lunar surface. J. Geophys. Res.: Space Phys. 118 (7), 3937–3945. (URL: ⟨http://dx.doi.org/10.1002/jgra.50337⟩).

Wieser, M., Barabash, S., Futaana, Y., Holmström, M., Bhardwaj, A., Sridharan, R., Dhanya, M., Schaufelberger, A., Wurz, P., Asamura, K., 2010. First observation of a mini-magnetosphere above a lunar magnetic anomaly using energetic neutral atoms. Geophys. Res. Lett. 37 (5).

Wieser, M., Barabash, S., Futaana, Y., Holmström, M., Bhardwaj, A., Sridharan, R., Dhanya, M., Wurz, P., Schaufelberger, A., Asamura, K., 2009. Extremely high reflection of solar wind protons as neutral hydrogen atoms from regolith in space. Planet. Space Sci. 57 (14–15), 2132–2134. (URL:⟨http://www.sciencedirect.com/science/article/pii/S0032063309002748 http://dx.doi.org/http://dx.doi.org/10.1016/j.pss.2009.09.012⟩.).

Xie, L., Zhang, X., Zheng, Y., Guo, D., 2016. Solar wind-generated current in the lunar dust experiment. Geophys. Res. Lett. 43 (8). http://dx.doi.org/10.1002/2016GL068640.